Numerical study of HCl and SO2 impact on sodium emissions in pulverized-coal flames

Kaidi Wan, Zhihua Wan, Jun Xia, Luc Vervisch, Pascale Domingo, Yu Lv, Yingzu Liu, Yong He, Kefa Cen

Numerical study of HCl and SO_2 impact on sodium emissions in pulverized-coal flames

Kaidi Wan[1], Zhihua Wang[2,*], Jun Xia[3,*], Luc Vervisch[1], Pascale Domingo[1], Yu Lv[4], Yingzu Liu[2], Yong He[2], Kefa Cen[2]

1. CORIA – CNRS, Normandie Université,
INSA de Rouen, 76800 Saint-Etienne-du-Rouvray, France

2. State Key Laboratory of Clean Energy Utilization,
Zhejiang University, Hangzhou 310027, China

3. Department of Mechanical and Aerospace Engineering & Institute of Energy Futures,
Brunel University London, Uxbridge UB8 3PH, UK

4. Department of Aerospace Engineering, Mississippi State University,
Mississippi State, MS 39762, USA

* Corresponding authors: wangzh@zju.edu.cn (Zhihua Wang); jun.xia@brunel.ac.uk (Jun Xia).

Abstract

Sodium emissions during pulverized-coal combustion (PCC) are known to result in severe ash-related operating issues of coal furnaces, e.g., fouling, slagging and corrosion. To relieve these issues and advance the clean utilization technologies of coal, a better understanding of the fundamental mechanisms driving the formation and transformation of the sodium species is required. In the present study, sodium emissions have been simulated in both one-dimensional (1D) premixed/diffusion flames of the coal volatile and an early-stage two-dimensional (2D) pulverized-coal flame. The properties of Loy Yang brown coal are used. The DRM22 skeletal mechanism is employed for volatile-gas combustion, and the reaction of sodium species is modeled by a detailed mechanism encompassing the elements Na, C, H, O, S and Cl. The compositions of the volatile fuels are obtained from the chemical percolation devolatilization (CPD) model, including CH_4, C_2H_2, CO, H_2, CO_2 and H_2O. The initial species of Na, Cl and S in the volatile gas is set to be NaOH, HCl and SO_2, respectively. The transformation characteristics of 12 sodium species are investigated in both the 1D volatile flames and the 2D pulverized-coal flame. The response of the sodium chemistry to volatile-gas combustion is analyzed under fuel-lean, stoichiometric and

fuel-rich conditions. Na, NaOH and NaCl are found to be the major sodium species during the combustion. Parametric studies with HCl, SO_2 or both species removed from the volatile are then performed to investigate their effects on the sodium transformation characteristics in both the 1D and 2D flames. The results show that HCl has a much stronger ability to react with sodium species than SO_2.

Keywords: Pulverized-coal combustion; Emission; Sodium chemistry; Alkali metal; HCl; SO_2

1. Introduction

Coal has been widely utilized to support the worldwide electric power consumption due to the overall flexibility of coal combustion systems [1]. In the near future, coal will continually play a major role in the energy structure of the world, considering its broad availability [2]. In practical utilization of coal, alkali metals such as sodium (Na) presented in coals lead to severe ash-related operating issues, e.g., fouling, slagging and corrosion [3]. This issue is also found in the combustion of biomass, which is a promising renewable energy source [4]. Potassium (K), an important element for plants, is usually rich in biomass. The alkali metal, i.e., Na and K, released from the combustion of coal and biomass can condense on heat transfer surfaces and form an initial sticky layer, which captures fly ash and leads to rapid ash deposition [5, 6]. Besides, alkali metal can also react with sulfur and chlorine species to form complex compounds, which causes fouling and corrosion of the furnaces [7]. These alkali metal emissions significantly limit the utilization of potassium-rich biomass such as straw and sodium-rich coals such as North Dakota coal in the US, Loy Yang coal in Australia and Zhundong coal in China [8]. Thus, to develop appropriate control technologies of reducing or capturing these harmful alkali metal emissions, it is essential to better understand the fundamental mechanisms driving the formation and transformation of alkali species and their interactions with the complex multi-phase turbulent reacting flows during the combustion of

pulverized coal and biomass.

In the past decades, experimental research on sodium release and reacting dynamics evolves from offline measuring techniques to online measurements using advanced laser diagnostics. Offline sampling measurements can obtain the final amount and composition of sodium species by analyzing the fly ash and ash deposits in the post-combustion stage [9]; while online techniques, e.g., planar laser-induced fluorescence (PLIF) [10, 11] and laser-induced breakdown spectroscopy (LIBS) [11-13], can directly capture the time-resolved sodium release process during the combustion. In our recent study, the dynamic release of atomic and elemental sodium during the combustion of a Zhundong coal pellet has been quantitatively measured by using PLIF [14] and multi-point LIBS methods [15], respectively.

On the numerical side, van Eyk et al. [16] firstly proposed a one-step Arrhenius sodium release model during the combustion of a single char pellet. A two-step kinetics model has been developed in our recent study [14, 15] to quantify the sodium release during all stages of coal combustion, based on simultaneous online measurements of the sodium release, pellet diameter and surface temperature of a burning coal pellet. Since the burnout time and coal pellet diameter in these studies are on the same order of magnitude as in a typical circulating fluidized bed (CFB) boiler, these sodium release models are appropriate for CFB combustion [15]. Sodium release models for pulverized-coal combustion (PCC) must still be developed.

Considering the homogeneous chemical reactions of alkali species, the final forms of alkali species in post-combustion gases can be modeled via thermodynamic equilibrium calculation, e.g. [15, 17, 18]. It has been found that the main alkali species are atomic Na/K, NaOH/KOH and NaCl/KCl in equilibrium [18]. Alkali chlorides can lead to severe ash deposition and corrosion issues, and a feasible method to mitigate these issues is to convert the alkali chlorides to sulfates, whose

75 melting temperatures are higher and which are therefore less problematic [19]. Hence, the
76 homogeneous chemical reaction, especially the sulfation of alkali has received more and more
77 attentions recently, e.g. [20-22]. Glarborg and Marshall [20] proposed a detailed chemical reaction
78 mechanism for homogeneous alkali reactions, which was validated against experimental results on
79 sulfation of gaseous alkali chlorides. Takuwa and Naruse [23] investigated the transformation
80 characteristics of gaseous sodium compounds in a hydrogen-air combustion system via
81 zero-dimensional (0D) isothermal simulations. However, the homogeneous reaction dynamics of
82 alkali species in a pulverized-coal flame has not been reported yet.

83 As the sharp increase of computing capacity continues, computational fluid dynamics (CFD)
84 methods for the carrier-gas flow of PCC have evolved from Reynolds-averaged Navier-Stokes
85 (RANS) simulation (e.g. [24-26]) towards high-fidelity approaches, i.e., large-eddy simulation (LES,
86 e.g. [27-34]) and direct numerical simulation (DNS, e.g., [35-37]). The high-fidelity approaches of
87 LES and DNS have demonstrated advantages over RANS in predicting local distributions of gas
88 temperature and species concentrations. Particularly in DNS, the turbulence-chemistry interaction is
89 directly resolved instead of being modeled, the simulation results can therefore provide more
90 physical insights into complex PCC dynamics and also serve as important data references for the
91 development of subgrid scale modeling.

92 In summary, the transformation dynamics of sodium species in a pulverized-coal flame have not
93 been fully revealed by previous studies. Within this context, the objective of the present study is
94 twofold. First, the responses of sodium species to one-dimensional (1D) premixed/diffusion flames
95 of coal volatile are investigated. Second, the transformation characteristics of sodium species in a
96 two-dimensional (2D) early-stage pulverized-coal flame are simulated and analyzed, excluding char
97 combustion. In our previous studies [34, 37], the reaction dynamics of sodium species in PCC were

98 investigated using a subset sodium mechanism without considering the effects of S and Cl. Here, the
99 full detailed sodium mechanism proposed by Glarborg and Marshall [20] including the elements Na,
100 C, H, O, S and Cl is employed to model the sodium reactions, and the effects of HCl and SO_2 on the
101 sodium transformation characteristics are then investigated. It should be noted that the detailed
102 sodium mechanism has been carefully validated by Glarborg and Marshall [20] against the
103 experimental results of the gas-phase sulfation of alkali chloride at combustion conditions [38].
104 It was found in [34, 37] that the multidimensional two-phase pulverized-coal flame showed a
105 partially premixing combustion mode, with first the premixed combustion mode dominating when
106 pulverized-coal particles are heated and ignited in the shear layer region where the high-temperature
107 co-flow mixes with the low-temperature air flow carrying pulverized-coal particles. After ignition
108 stabilizes, volatile fuels are rapidly released from pulverized-coal particles, leading to a dominantly
109 diffusion burning mode. In view of this fact, in order to better understand how minor sulfur and
110 chlorine species affect sodium emissions in pulverized-coal flames, it will be instructive to first
111 investigate prototype one-dimensional premixed and diffusion gaseous flames of the coal volatile
112 using detailed chemistry, leaving behind the complexity of interactions between dispersing
113 pulverized-coal particles and the gas phase, turbulent flow effects, etc. This inspection will provide a
114 first guiding light on S/Cl-affected sodium emissions in both the prototype premixed and diffusion
115 volatile flames. By comparing the one-dimensional prototype gaseous volatile flames and a more
116 realistic multidimensional two-phase pulverized-coal flame, a comprehensive understanding of
117 sodium emissions impacted by minor sulfur and chlorine species can be obtained.

118 **2. One-dimensional premixed/diffusion flames of coal volatile**

119 The reaction dynamics of sodium species in 1D premixed/diffusion flames of coal volatile is
120 studied. The volatile is released from the Loy Yang brown coal [17], for which the coal analysis data

121 are shown in Table 1. The volatile combustion is modeled by the previously validated DRM22
122 skeletal mechanism proposed by Kazakov and Frenklach [39], involving 22 chemical species and
123 104 elementary reactions. The compositions of the volatile fuels are obtained from the chemical
124 percolation devolatilization (CPD) model [40] and the Tar species is replaced by C_2H_2 [32], as shown
125 in Table 2. The compositions predicted by the CPD model have been slightly adjusted to fulfill the
126 elemental mass conservation.

127 According to [23], the initial species of Na in the volatile is set to be NaOH, while those of Cl
128 and S are set to be HCl and SO_2, respectively. The percentage of sodium that is releasable during the
129 coal pyrolysis stage is set to 19.1%, according to the experimental data [17]. However, the release of
130 sulfur and chlorine has not been measured. Considering sulfur and chlorine can be fully released
131 during the pyrolysis and char burning stages of coal combustion, their releasable proportions during
132 the pyrolysis stage are both set to 55.1%, which is the percentage of volatile yields predicted by the
133 CPD model. The mass fractions of NaOH, HCl and SO_2 in the volatile gas can then be calculated
134 (see Table 2). The detailed reaction mechanism of alkali metal species developed by Glarborg and
135 Marshall [20] includes elementary reactions over the elements Na, K, C, H, O, S and Cl. In the
136 present study, since the concentration of potassium in the coal is an order of magnitude lower than
137 that of sodium (see Table 1), the element K is not considered, which results in a detailed reaction
138 mechanism of sodium involving 36 species and 153 elementary reactions.

139 Table 1. Analysis of Loy Yang brown coal [17].

Dry basis, wt%	
C	67.8
H	5.20
N	0.57
S	0.24
Cl	0.06
Ash	0.80

O	25.3
In ash, wt%	
SiO_2	12.9
Al_2O_3	31.4
Fe_2O_3	6.70
TiO_2	0.70
K_2O	0.77
MgO	12.2
Na_2O	11.3
CaO	5.60
SO_3	16.9

Table 2. Modeled volatile-gas compositions of Loy Yang brown coal.

Hydrocarbon volatile compositions predicted by the CPD model (mass fractions)					
CH_4	C_2H_2	CO	H_2	CO_2	H_2O
0.03707	0.30698	0.20664	0.02976	0.15394	0.25979
Non-hydrocarbon volatile compositions (mass fractions)					
NaOH	HCl	SO_2			
4.0E-4	6.2E-4	48.0E-4			

For the premixed condition, a 1D freely propagating premixed flame of the volatile is simulated using CANTERA [41]. Three equivalence ratios (ϕ = 0.5, 1.0 and 2.0) of the volatile-air mixture are considered and the inlet mixture temperature is 300 K. The equivalence ratio is computed based on the molar fractions of atomic carbon, hydrogen and oxygen [34, 37], which is therefore conserved during homogeneous combustion but not conserved during mixing. For the diffusion condition, a 1D counterflow diffusion flame of the volatile is simulated using CANTERA [41]. The mass flow rates of the volatile fuel and air inlets are 0.024 (kg/m^2 s) and 0.072 (kg/m^2 s), respectively, while the temperatures of both inlets are 300 K. To investigate the effects of HCl and SO_2 on sodium transformation characteristics, four different configurations with HCl and/or SO_2 removed are set up. The removed HCl/SO_2 is replaced by N_2. In total 16 cases are simulated with the three equivalence ratios in the premixed condition and different configurations of HCl and SO_2 in both the premixed

and diffusion conditions. The grid is limited to 250 points and the 1D domain length for premixed and diffusion flame is 1.0 m and 3.0 cm, respectively.

3. Pulverized-coal flame configuration and numerics

A two-dimensional temporally evolving pulverized-coal jet flame is studied (Fig. 1). The physical dimensions of the computational domain are 51.2 mm and 51.2 mm in the streamwise (x) and spanwise (y) directions, respectively. A uniform mesh of h = 100 μm is employed, which has been shown to be able to resolve the flame structure [37]. High-speed air (bulk velocity: 10 m/s, 300 K) laden with pulverized-coal particles is initially set up for $|y| < 2.5$ mm. The initial number of particles is 171 and their locations follow a random uniform distribution. The initial density of particles is 1400 kg/m^3 with a mono-disperse distribution of diameter of 25μm. Properties of Loy Yang brown coal [17] are employed (Table 1). A low-speed hot burnt product of the hydrocarbon volatile at an equivalence ratio of 0.45 (3 m/s, 1559 K) is introduced as the coflow surrounding the air. The coflow stream promotes the ignition of coal particles, as the mixing of the solid-fuel/air mixture with burnt products would do in a real pulverized-coal furnace. Periodic boundary conditions are introduced in all directions. To facilitate the jet flow development, turbulent fluctuations of 0.2 m/s (2% of the primary air velocity) are initially set within the shear layers between the primary air and the coflow. The parameters of the present case are chosen according to [37]. Pulverized-coal particles are treated as point sources and two-way coupling between the gas phase and particles are considered.

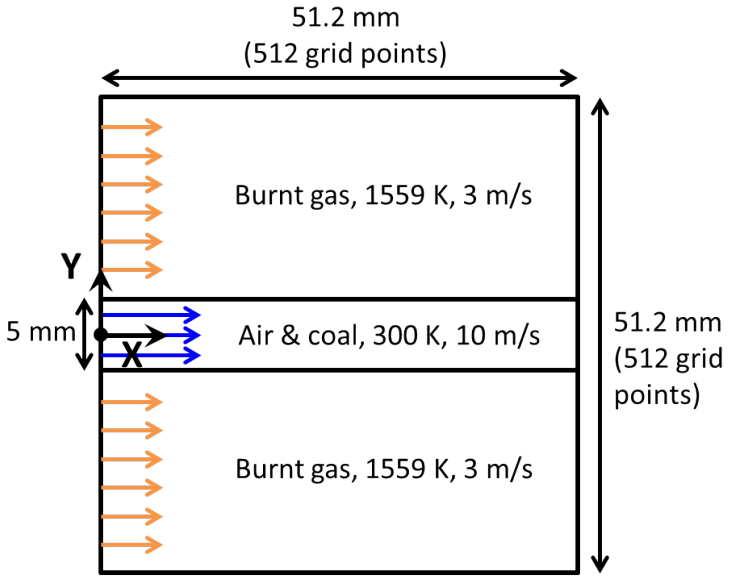

Figure 1. Schematic diagram of computational configuration.

Coal pyrolysis, including Na/Cl/S release, volatile-gas combustion and Na/Cl/S reactions are simulated. Heterogeneous reaction of char is not considered, because its contribution is weak in a small-scale pulverized-coal flame, as already demonstrated in [32, 34, 42].

3.1. Gas phase modeling

The governing equations for the gas and coal-particle phases are solved in the Eulerian and Lagrangian frameworks, respectively, using a low-Mach-number in-house code [30, 33, 34, 37]. The conservation equations for mass, momentum, species and temperature are solved for the gas phase:

$$\mathrm{D}_t \rho = \dot{S}_{m,p} \tag{1}$$

$$\mathrm{D}_t \left(\rho u_i \right) = -\partial_i p + \partial_j \tau_{ij} + \dot{S}_{mom,p,i} \tag{2}$$

$$\mathrm{D}_t \left(\rho Y_n \right) = \partial_j \left(\rho D_n \partial_j Y_n \right) + \dot{\omega}_{Y,n} + \dot{S}_{Y,p,n} \tag{3}$$

$$\mathrm{D}_t \left(\rho T \right) = \partial_j \left(\frac{\lambda}{C_{P,g}} \partial_j T \right) + \frac{\lambda}{C_{P,g}^2} \partial_j C_{P,g} \partial_j T + \dot{\omega}_T + \dot{S}_{T,p} + \dot{S}_{T,R} \tag{4}$$

where $\mathrm{D}_t(\Phi) = \partial_t(\Phi) + \partial_j(\Phi u_j)$, $\partial_j \equiv \partial x_j$, ρ is gas density (kg/m^3), u_i is gas velocity (m/s), Y_n is the mass fraction of the nth chemical species, T is gas temperature (K). The pressure is denoted by p, and $\tau_{ij} = \mu(\partial_j u_i + \partial_i u_j - 2/3\ \partial_k u_k \delta_{ij})$ is the viscous stress tensor. D_n is the molecular mass diffusivity coefficient (m^2/s), λ and $C_{P,g}$ are the thermal conductivity (W/m K) and specific heat capacity (J/kg K)

of the gas mixture, respectively. $\dot{S}_{m,p}$, $\dot{S}_{mom,p,i}$, $\dot{S}_{Y,p,n}$ and $\dot{S}_{T,p}$ are the two-way coupling terms due to the effects of particles on the gas phase. $\dot{\omega}_{Y,n}$ is the chemical reaction source term due to homogeneous reaction. In the temperature equation, the radiative heat transfer ($\dot{S}_{T,R}$), heat exchange between the gas phase and coal particles ($\dot{S}_{T,p}$), and heat effects of homogeneous reaction ($\dot{\omega}_T$) are considered. In the present study, the Lewis number (Le = 1.0) and Prandtl number (Pr = 0.7) are assumed to be constant.

3.2. Particle phase modeling

The momentum equation of a Lagrangian coal particle can be written as:

$$\mathrm{d}_t u_{p,j} = f\left(u_j - u_{p,j}\right)/\tau_p \tag{5}$$

where $u_{p,j}$ is the velocity of the particle (m/s). The dynamic response time (s) of a particle is $\tau_p = \rho_p d_p^2/18\mu$, where ρ_p is the particle density (kg/m^3), and d_p is the particle diameter (m). f is the drag coefficient, accounting for the high particle Reynolds number effects and the blowing effects of volatiles at the particle surface [43].

The particle temperature equation is:

$$\mathrm{d}_t T_p = \left(Q_{conv} + Q_{rad} + Q_{dev}\right)/\left(m_p C_{P,p}\right) \tag{6}$$

where T_p is the temperature of the particle (K), m_p mass of the particle (kg), $C_{P,p}$ specific heat capacity of the particle (J/kg K). The heat transfer due to convection, radiation, and pyrolysis (devolatilization) is $Q_{conv} = \mathrm{Nu} C_{P,g} m_p \left(T - T_p\right)/3\,\mathrm{Pr}\,\tau_p$, $Q_{rad} = \varepsilon_p \pi d_p^2 \sigma\left(T_R^4 - T_p^4\right)$, and $Q_{dev} = -\Delta h_{dev}\,\mathrm{d}m_{vol}/\mathrm{d}t$, respectively. Nu is the Nusselt number and calculated by the Ranz-Marshall correlations [44]. The radiation temperature (K) is estimated by $T_R = (G/4\sigma)^{1/4}$, where G is the incident radiation (W/m^2) determined by the Discrete Ordinates Method (DOM) [45]. σ is the Stefan-Boltzmann constant (5.67×10^{-8} W/m^2 K^4). ε_p is the particle emissivity and set to 0.9 [46]. The weighted-sum-of-the-gray-gases model (WSGGM) [47] is employed to determine the gas

213 absorption coefficient. Finally, the mass loss rate of each coal particle (dm_p/dt), due to the pyrolysis,
214 is directly predicted by the CPD model, as in [30, 33, 34].

215 *3.3. Gas phase chemistry*

216 The gas phase chemistry employed here is the same as that in Section 2. The homogeneous
217 combustion of the hydrocarbon volatile and the sodium species reaction are modeled by the DRM22
218 skeletal mechanism [39] and the detailed alkali reaction mechanism [20], respectively. The
219 compositions of the volatile gas including the non-hydrocarbon compounds of Na, S and Cl can be
220 found in Table 2.

221 The release rate of sodium of pulverized-coal is assumed to be proportional to the volatile
222 release rate [34, 37], because the sodium vapor generated inside the porous structure of a coal
223 particle will be transported outward by the volatile yielded during the pyrolysis stage and the sodium
224 release was found proportional to the burnout of a coal particle during the early combustion stage
225 [15]. Similarly, the release rates of sulfur and chlorine are also assumed to be proportional to the
226 volatile release rate.

227 *3.4. Numerical schemes*

228 The numeric of our in-house code is based on an approach previously employed for both DNS
229 and LES [48, 49]. A second-order Crank-Nicolson scheme is used for the time advancement. A
230 second-order central difference scheme is applied to all terms in the momentum equation and the
231 scalar diffusion terms in the species and temperature equations. To secure the scalar boundedness, a
232 Quadratic Upstream Interpolation for Convective Kinematics (QUICK) scheme is employed for the
233 scalar advection terms in the species and temperature equations. An Alternating Direction Implicit
234 (ADI) method has been used, and therefore semi-implicit tridiagonal/pentadiagonal equations are
235 solved separately for each direction. A second-order Runge-Kutta (RK2) scheme is used to explicitly

236 advance the particle equations.

237 **4. Results and discussion**

238 *4.1. Transformation characteristics of sodium species in 1D premixed flame*

239 To investigate the transformation characteristics of sodium species under different burning
240 conditions, the reactions of sodium species in 1D freely propagating volatile flames have been
241 simulated for three equivalence ratios (ϕ = 0.5, 1.0 and 2.0), which are selected to illustrate fuel-lean,
242 stoichiometric and fuel-rich conditions. As shown in Fig. 2, the concentration of NaOH rapidly
243 decreases after the volatile mixture is injected through the inlet, which is due to the following two
244 reaction paths. First, $Na_2O_2H_2$ is produced by $2NaOH \rightarrow Na_2O_2H_2$. Second, NaOH reacts with HCl
245 in the volatile gas by $NaOH + HCl \rightarrow NaCl + H_2O$, and NaCl subsequently forms Na_2Cl_2 via $2NaCl$
246 $\rightarrow Na_2Cl_2$. It can be found that $Na_2O_2H_2$ and Na_2Cl_2 are the two major sodium species in the initial
247 unburned region with T = 300 K. In the combustion region where the gas temperature rapidly
248 increases, $Na_2O_2H_2$ and Na_2Cl_2 are decomposed to NaOH and NaCl, respectively, and then
249 transformed to other sodium species, i.e., Na, $NaSO_2$, $NaHSO_4$ and Na_2SO_4. In the post-flame,
250 high-temperature flue-gas region, the sodium species are then gradually evolving towards the
251 equilibrium. All the sulfurous sodium species are consumed, and the atomic sodium Na is the most
252 significant sodium product (> 10 ppm) under stoichiometric and fuel-rich conditions while NaCl is
253 the main sodium product (> 10 ppm) under fuel-lean condition. H radical generated from the
254 hydrocarbon combustion helps to produce Na via the following two reaction paths: $NaOH + H \rightarrow Na$
255 $+ H_2O$ and $NaCl + H \rightarrow Na + HCl$. NaOH is another major sodium product which shows a
256 concentration of 1-10 ppm under different conditions. The other four minor sodium species, i.e.,
257 NaO, NaO_2, $NaSO_3$ and $NaSO_3Cl$, have a maximum concentration less than 0.5 ppm during the
258 whole reaction process for all the three equivalence ratios (not shown here).
259

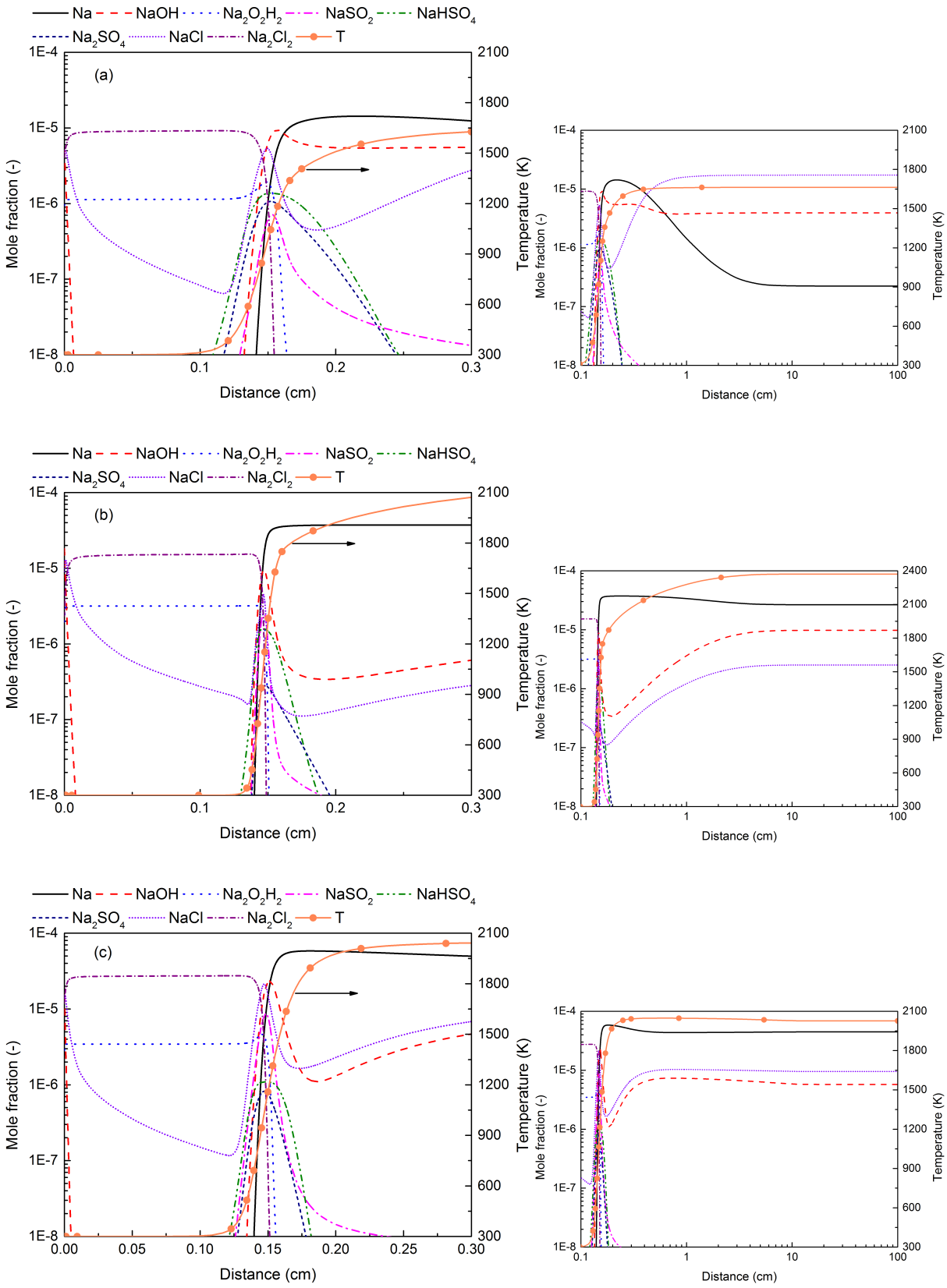

Figure 2. Sodium species distribution versus distance along the 1D premixed volatile flame at equivalence ratio ϕ = 0.5 (a), ϕ = 1.0 (b) and ϕ = 2.0 (c). The heat release zone is zoomed in and shown on the left side while the overall flame is shown on the right side.

To investigate the effects of HCl and SO_2 on sodium transformation characteristics, three additional configurations have been set up, which are Case B (HCl is removed from the volatile and

replaced by N_2), Case C (SO_2 is removed from the volatile and replaced by N_2) and Case D (both HCl and SO_2 are removed from the volatile and replaced by N_2). The original baseline case is referred to as Case A. For each case of A/B/C/D, three simulations are performed with ϕ = 0.5, 1.0 and 2.0. Figure 3 illustrates the comparison among the cases on the representative sodium species NaOH, NaCl and Na_2SO_4. The profiles are shown until Distance of 10 cm, since it can be found in Fig. 2 the sodium reactions almost reach equilibrium at this position. At the initial unburned region where Distance < 0.1 cm, HCl has a significant influence on the profile of NaOH, which is evident by comparing the cases with HCl involved (Cases A/C) and the cases without HCl (Cases B/D). With HCl presented, NaOH is consumed rapidly by HCl via NaOH + HCl → NaCl + H_2O, and the produced NaCl shows a similar profile to NaOH in the cases without HCl in the initial region, because the reaction kinetics of 2NaOH → $Na_2O_2H_2$ and 2NaCl → Na_2Cl_2 are similar. In the combustion and post-flame regions, the profiles of NaCl are similar for different cases while Na_2SO_4 is found to have a wider distribution when HCl is not presented (comparing Case A with B), especially under the fuel-lean condition. The characteristics of NaOH are more subtle. Under fuel-lean and fuel-rich conditions, NaOH is found to have a lower concentration in the sodium products when HCl is presented (Cases A/C), which should be attributed to NaOH + HCl → NaCl + H_2O. However, under stoichiometric condition, the profiles of NaOH become similar for the four cases since the mole fraction of NaCl is quite low, which means the transformation from NaOH to NaCl is not favored. Comparing the cases with SO_2 involved (Cases A/B) and the cases without SO_2 (Cases C/D), it can be found that the impact of SO_2 on representative sodium profiles such as NaCl and NaOH is minor.

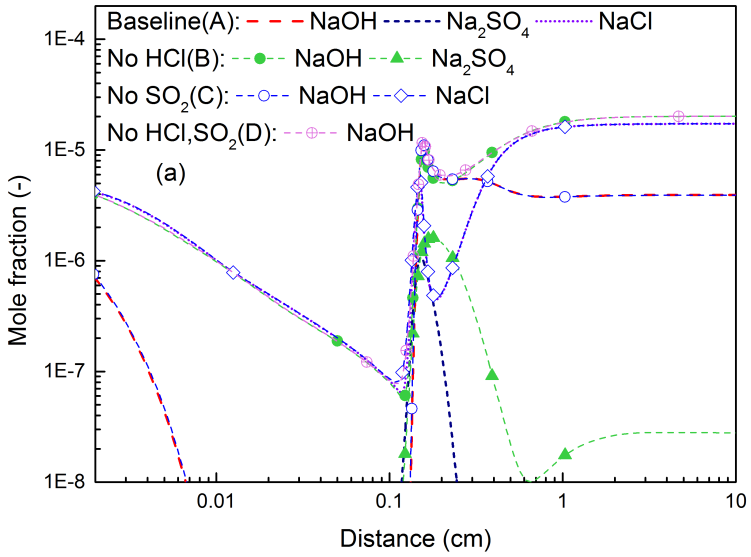

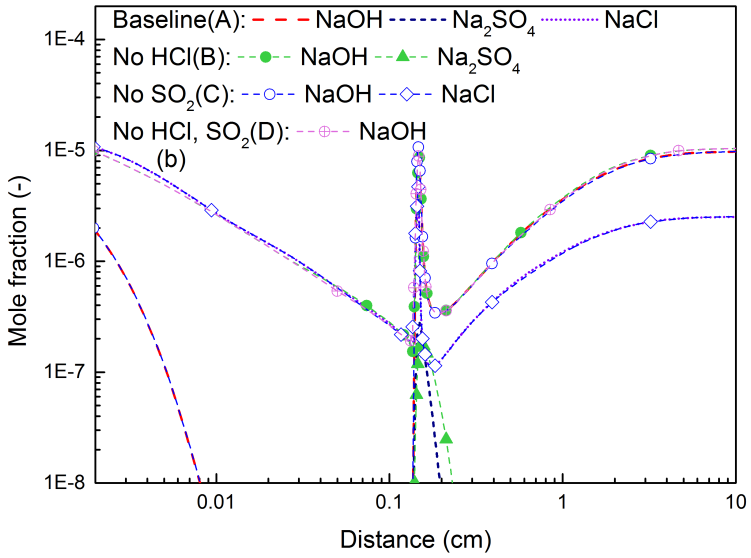

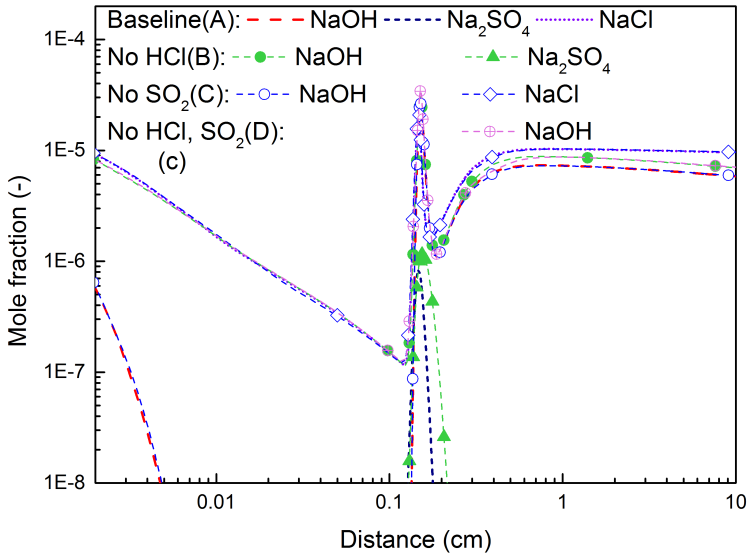

Figure 3. Comparison of sodium species distribution versus distance along the 1D premixed volatile flame between Case A (the baseline case), Case B (HCl removed), Case C (SO_2 removed) and Case D (both HCl and SO_2 removed) at equivalence ratio ϕ = 0.5 (a), ϕ = 1.0 (b) and ϕ = 2.0 (c).

300 *4.2. Transformation characteristics of sodium species in 1D diffusion flame*

301 To investigate the transformation characteristics of sodium species in diffusion flame, four cases
302 have been set up, which are Case E (the baseline case), Case F (HCl is removed from the volatile and
303 replaced by N_2), Case G (SO_2 is removed from the volatile and replaced by N_2) and Case H (both
304 HCl and SO_2 are removed from the volatile and replaced by N_2). Figure 4 shows the comparison
305 among the cases on the representative sodium species Na, NaOH, NaCl and Na_2SO_4. Here, only the
306 results of the mixture fraction $Z < 0.5$ are shown, because a higher mixture fraction is rarely observed
307 in the following 2D DNS study (see Fig. 8 below). The mixture fraction is defined as $Z = 1.0 -$
308 $Y_{N2}/0.767$. For the two-stream mixing, 1D diffusion flame, $Z = 1$ and $Z = 0$ indicate the coal-volatile
309 and oxidizer streams, respectively. The positions of ϕ = 0.5, 1.0 and 2.0 in the mixture fraction
310 coordinate are also indicated. It can be found that in all the four cases the mole fraction of Na
311 increases rapidly with Z in the fuel-lean region. In the fuel-rich region with $\phi > 2.0$, the profiles of
312 Na show a decreasing trend in the cases with HCl (Cases E/G), which is not observed in the cases
313 without HCl (Cases F/H). Both NaCl and NaOH have higher concentrations in fuel-lean and
314 fuel-rich regions while relatively low concentrations under the stoichiometric condition. HCl is also
315 found to decrease the concentrations of NaOH and Na in the fuel-rich region with $\phi > 2.0$. For
316 Na_2SO_4, it can reach a higher concentration when HCl is not presented but its mole fraction is still
317 below 1 ppm in the whole range of Z. Since the concentrations of sulfurous sodium species are quite
318 low, the effects of SO_2 on the profiles of Na, NaCl and NaOH are minor, as shown in the comparison
319 between the cases with SO_2 involved (Cases E/F) and the cases without SO_2 (Cases G/H).

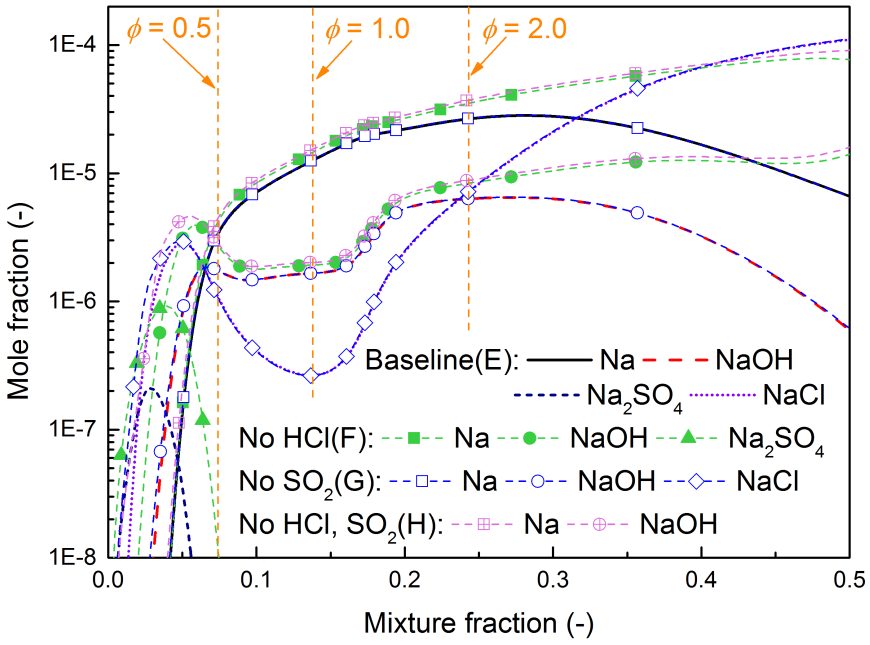

Figure 4. Comparison of sodium species distribution in the mixture fraction space of the 1D diffusion volatile flame among Case E (the baseline case), Case F (HCl removed), Case G (SO_2 removed) and Case H (both HCl and SO_2 removed).

4.3. Characteristics of the 2D pulverized-coal flame

The transformation characteristics of the sodium species in the 2D pulverized-coal flame are now examined. Figure 5 shows the instantaneous distributions of the (a) gas temperature and particle burnout, (b) OH mass fraction, (c) Na mass fraction, (d) NaCl mass fraction, and (e) flame index and particle temperature of the pulverized-coal flame. In the early stage, the coal particles in the jet shear layers are heated by the high-temperature coflow. Volatiles including sodium, sulfur and chlorine compounds are then released from the particles due to the pyrolysis. Isolated flame structures [27, 34] are observed at t = 10 and 15 ms. Some particles are ignited at first in the shear layers, but the heat release is not strong enough to ignite adjacent coal particles. At t = 20 ms, more and more particles are ignited and Y_{OH} propagates around them, indicating a strong heat release and rapid spreading of the flame. Atomic sodium Na reaches a high concentration in the high-temperature flame region, while NaCl accumulates around the ignited particles. With most of the coal particles in the computational domain burn out at t = 30 ms, the burning tends to be weaker, but a wider combustion regime can be found as the mixing continues. The mass fractions of OH radical and atomic Na are

decreasing, but NaCl achieves a high concentration.

The flame index, F.I., [35, 50] is calculated from the spatial gradients of the mass fractions of the volatile fuel and the oxidizer as: F.I. = $\nabla Y_f \cdot \nabla Y_{O2}$, where $Y_f = Y_{CH4} + Y_{CO} + Y_{C2H2} + Y_{H2}$. Positive values of F.I. probe premixed flame regimes, while negative ones indicate diffusion flame regimes. In Fig. 5e, the F.I. is shown in the regions where the heat release rate exceeds 10^6 W/m^3, which indicates active burning regions. The maximum heat release rate in the 2D domain is 1.28×10^{10} W/m^3. It can be found that the diffusion combustion mode dominates in the region around coal particles where high fluxes of volatile release locate, while the premixed regimes appears in the surrounding area with a lower concentration of volatile. To better illustrate the characteristics of the F.I. during the ignition process of coal particles, three continuous snapshots of the instantaneous distribution of the F.I. at t = 14.0, 14.5 and 15.0 ms are shown in Fig. 6. It can be observed that the first ignition of coal particles is controlled by homogeneous combustion and thus dominated by premixed regimes. As the volatile around particles are ignited, the particles are heated rapidly by the surrounding flame. The volatile release is then enhanced, which allows for the fuel to accumulate before burning and therefore leads to a dominant diffusion combustion mode.

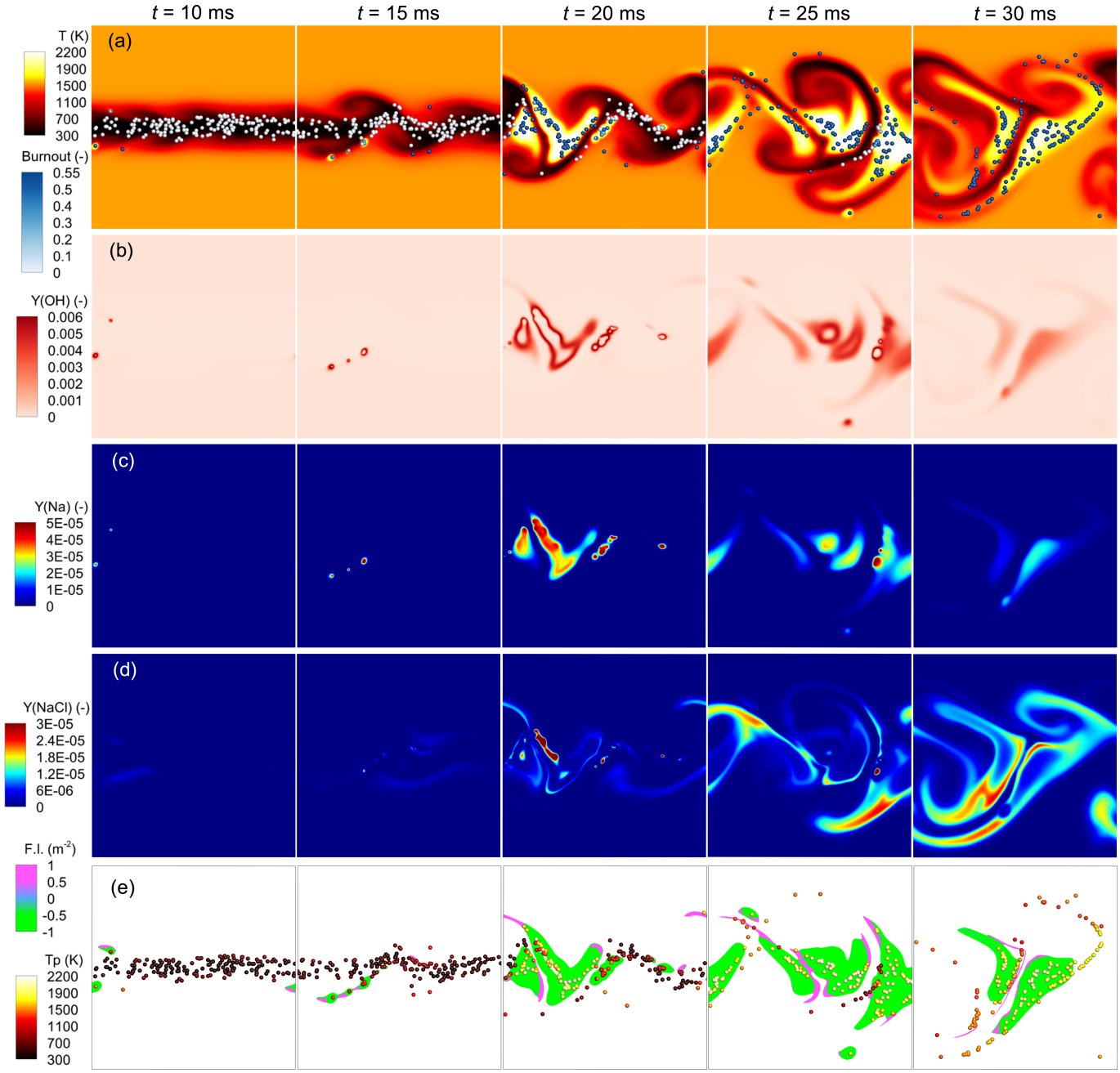

Figure 5. Time evolutions of instantaneous distributions of the (a) gas temperature and particle burnout, (b) OH mass fraction, (c) Na mass fraction, (d) NaCl mass fraction and (e) flame index and particle temperature.

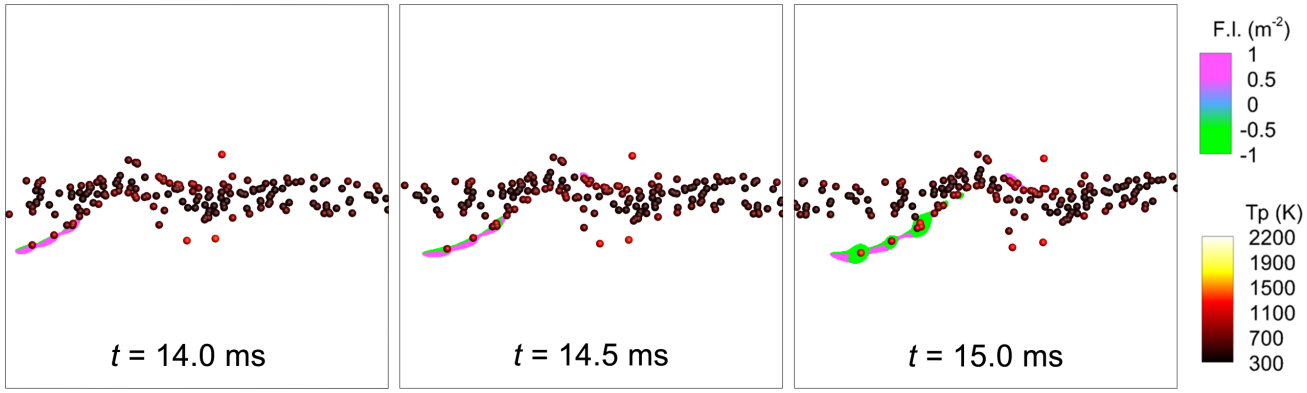

Figure 6. Time evolutions of instantaneous distribution of the flame index and particle temperature from t = 14.0 ms to t = 15.0 ms.

Figure 7 shows the instantaneous distributions of the mass fractions of all the twelve sodium species in the DNS at t = 20 ms, along with the distributions of the equivalence ratio ϕ and the mass fractions of HCl and SO_2. High values of ϕ are induced by the volatile stream released from coal particles. The isoline of ϕ = 1 superimposed in Fig. 7 represents the stoichiometric conditions for reactions between the volatile and the oxidizer. It can be found that both HCl and SO_2 are mainly located in the fuel-rich (inside the isoline) region, as they are released simultaneously with the volatile stream. For the sodium species, atomic Na is also found to have a high concentration in the fuel-rich region, which is in accordance with our previous study [34, 37]. Both NaOH and NaCl feature a high concentration in the fuel-rich region, a moderate concentration in the fuel-lean region (outside the isoline), while a low concentration in the stoichiometric region. Since NaOH is the released sodium species along with the volatile, the reaction $NaOH + HCl \rightarrow NaCl + H_2O$ explains the high concentration of NaCl in the fuel-rich region. $NaHSO_4$ and Na_2SO_4 are the two main sulfated sodium species, but their concentrations are much lower than that of NaCl. It can be observed that the two sulfated sodium species mainly form in the fuel-lean region, similar to Na_2Cl_2 and $Na_2O_2H_2$, which are favored sodium species in the pre-combustion mixture. The other five minor sodium species, i.e., NaO, NaO_2, $NaSO_2$, $NaSO_3$ and $NaSO_3Cl$, are also found to be produced under the fuel-lean condition, except that $NaSO_2$ is also largely generated in the fuel-rich region where abundant sodium and sulfur exist.

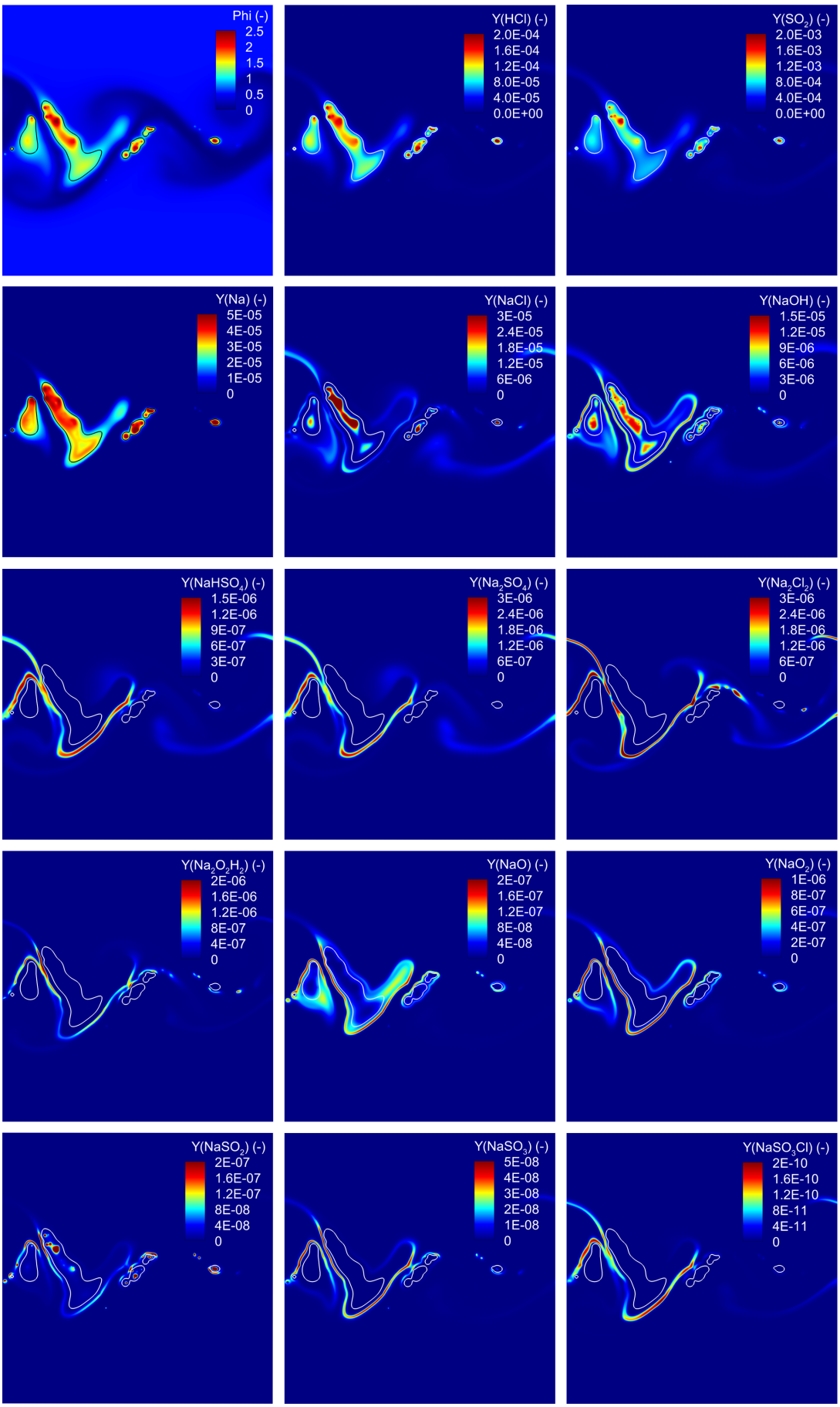

Figure 7. Instantaneous distributions of the equivalence ratio (ϕ), the mass fractions of HCl, SO_2 and all the twelve sodium species at t = 20 ms. The isoline of ϕ = 1 is superimposed.

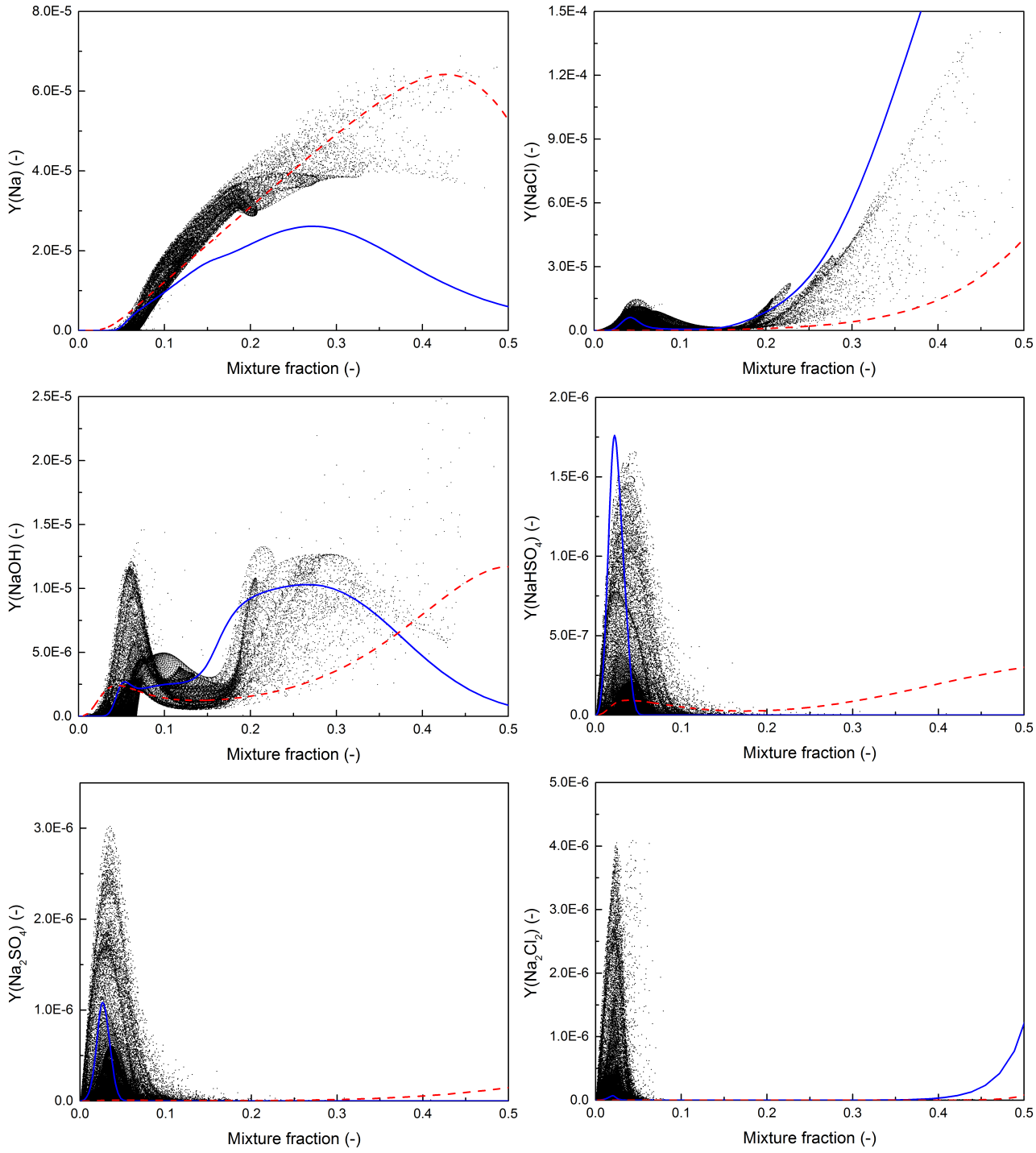

Figure 8. Scatter plots of instantaneous mass fractions of Na, NaCl, NaOH, $NaHSO_4$, Na_2SO_4 and Na_2Cl_2 against Z at t = 20 ms. Blue solid line and red dash line are the sodium profiles obtained from 1D counterflow diffusion flames, corresponding to the lowest (23 s^{-1}) and highest strain rates (11318 s^{-1}).

4.4. Sodium species dynamics

Figure 8 shows the scatter plots of instantaneous mass fractions of six sodium species against the mixture fraction, Z, at t = 20 ms. For the three-stream mixing, 2D pulverized-coal flame, the mixture fractions of the volatile released from pulverized-coal particles (the fuel stream), the air jet

393 which carries pulverized-coal particles (the oxidizer stream) and the high-temperature coflow are Z =
394 1, Z = 0 and Z = 0.068, respectively. Na, NaCl and NaOH are found to be the three major sodium
395 species in the reaction products. Y_{Na} stays almost zero in the range of $Z < 0.05$, and then increase
396 rapidly with Z. The distributions of Y_{NaCl} and Y_{NaOH} are subtler. Their mass fractions reach the first
397 peak around Z = 0.05, then decrease to a much lower value under the stoichiometric condition of Z_{st}
398 = 0.138, then increase again for higher Z and reach a much higher value under the fuel-rich condition
399 than the first peak. Finally, Y_{NaHSO4}, Y_{Na2SO4} and Y_{Na2Cl2} feature a single-peak distribution within the
400 fuel-lean regime of $Z < 0.138$, similar to the mass fractions of other sodium species, i.e., $Y_{Na2O2H2}$,
401 Y_{NaO}, Y_{NaO2}, Y_{NaSO3}, $Y_{NaSO3Cl}$ (not shown here). The distribution of Y_{NaSO2} is similar to Y_{NaCl}, which
402 has higher values both in the fuel-lean and fuel-rich regimes (not shown here).

403 The blue solid line and the red dash line in Fig. 8 are the sodium profiles obtained from 1D
404 counterflow diffusion flames, corresponding to the lowest and highest strain rates, respectively. The
405 high-strain rate (red dash line) slow down the consumption of NaOH and the production of $NaHSO_4$
406 and Na_2SO_4 in the fuel-lean regime. The generation of NaCl is also limited under the high-strain rate,
407 but the generation of atomic Na is found to be promoted. Compared with the sodium profiles from
408 1D counterflow diffusion flames, the DNS scatters basically follow a similar trend, but many data
409 points fall outside the region between the two profiles corresponding to the lowest and highest strain
410 rates. These points are likely to be representative of unsteadiness and/or partial premixing of the
411 reactants, since the volatile, after being ejected from the particles, and the ambient air are rapidly
412 mixed in a partially premixed mode, as in [51]. In addition, the radiation heat loss also contributes to
413 the mismatch between DNS scatters and profiles from 1D diffusion flames.

414 *4.5. Statistics of the 2D pulverized-coal flame*

415 Figures 9 and 10 show the time evolutions of the averaged mass fractions of OH, HCl, SO_2, Z_{vol}

and six sodium species, and the averaged gas temperature of the 2D pulverized-coal flame, all of which are calculated as the mean over the 2D computational domain. Z_{vol} is the volatile mixture fraction, which is obtained from the following equation:

$$\mathrm{D}_t\left(\rho Z_{vol}\right)=\partial_j\left(\rho D_Z \partial_j Z_{vol}\right)+\dot{S}_{Y,p,vol} \tag{7}$$

where D_Z is the diffusivity coefficient of volatile (m^2/s) and is set equal to the thermal diffusivity coefficient. $\dot{S}_{Y,p,vol}$ is the source term of the mass of the volatile released from coal particles.

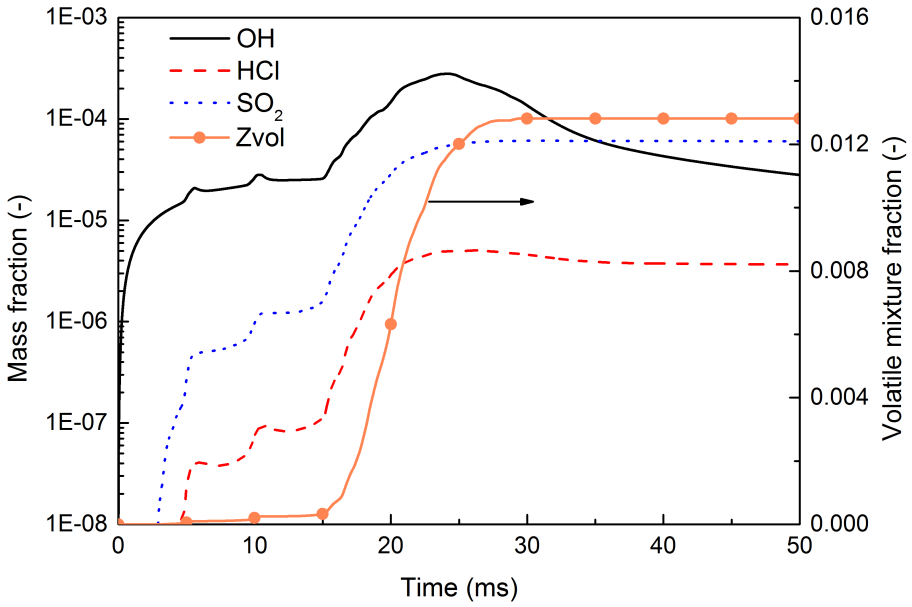

Figure 9. Time evolutions of the mean mass fractions of OH, HCl, SO_2 and Z_{vol} averaged over the 2D computational domain.

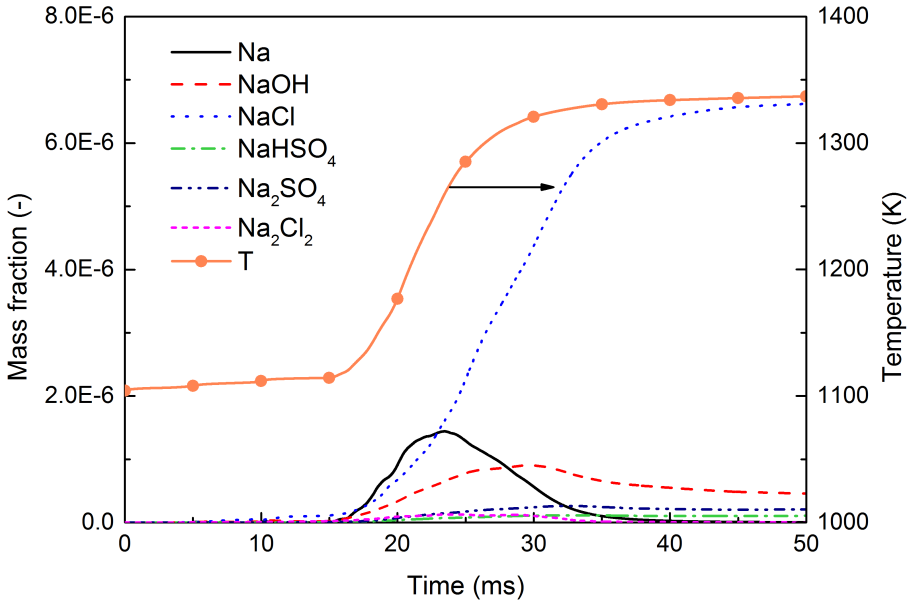

Figure 10. Time evolutions of the averaged mass fractions of Na, NaOH, NaCl, $NaHSO_4$, Na_2SO_4 and Na_2Cl_2, and the averaged gas temperature.

At t = 5 and 10 ms, small peaks can be observed for Y_{OH}, Y_{HCl} and Y_{SO2}, and also for the mass fractions of sodium species in log-scale (not shown here). This is because the volatile around some coal particles is ignited and the flame heats the particles rapidly, which therefore leads to a high flux of volatile release. After t = 15 ms, both Z_{vol} and T increase rapidly, which indicates the pulverized-coal jet is actively burning. The mass fractions of Y_{OH}, Y_{HCl}, Y_{SO2}, Y_{Na} and Y_{NaCl} also start to significantly increase after t = 15 ms. After t = 30 ms, both Z_{vol} and T remain almost constant, indicating that the volatile release and homogeneous combustion have both ended. However, although the averaged gas temperature remains after t = 30 ms, the variance of the gas temperature in the domain decreases due to the turbulent mixing of the hot products and the surroundings. It explains the variation of the species mass fractions after t = 30 ms, e.g. the decreasing Y_{HCl}, which should be attributed to the reaction NaOH + HCl → NaCl + H_2O. At the end of the simulation (t = 50 ms), NaCl is found to be the major sodium product while the other sodium species are minor.

4.6. Effects of HCl and SO_2 on sodium emissions in the 2D pulverized-coal flame

To investigate the effects of HCl and SO_2 on sodium transformation characteristics, three additional DNS cases were set up, which are Case K (HCl is removed from the volatile), Case L (SO_2 is removed from the volatile) and Case M (both HCl and SO_2 are removed from the volatile). All the removed species are replaced by N_2. The original baseline DNS case is referred to as Case J. Figure 11 shows the comparison between the cases on the time evolution of the representative sodium species Na, NaOH, NaCl and Na_2SO_4. It can be found that without HCl and SO_2, NaOH is the main sodium product at the end of the simulation (Case M). When only HCl is included in the volatile, NaOH is largely consumed by HCl and NaCl forms as the main sodium product (Case L). If SO_2 is presented while HCl is not, NaOH is then partly transformed to Na_2SO_4, and both NaOH and Na_2SO_4 become the major sodium products (Case K). Interestingly, when both HCl and SO_2 are

presented (Case J), the reaction characteristics of the sodium species are very similar to Case L with HCl but no SO_2. It implies that SO_2 has only a minor contribution to the reactions with sodium species when HCl also exists in the released volatile. Hence, HCl has a much stronger ability to react with sodium species than SO_2. In view of the reaction paths, HCl reacts with sodium species in a straightforward way, e.g., HCl + NaOH → NaCl + H_2O and HCl + Na → NaCl + H. However, the reactions between SO_2 and sodium species are more complex. The SO_2 is first oxidized to SO_3, to then reacts with sodium species, e.g., NaOH, to form NaHSO4, and finally produce Na_2SO_4 via shuffle reactions, e.g., $NaHSO_4$ + NaOH → Na_2SO_4 + H_2O.

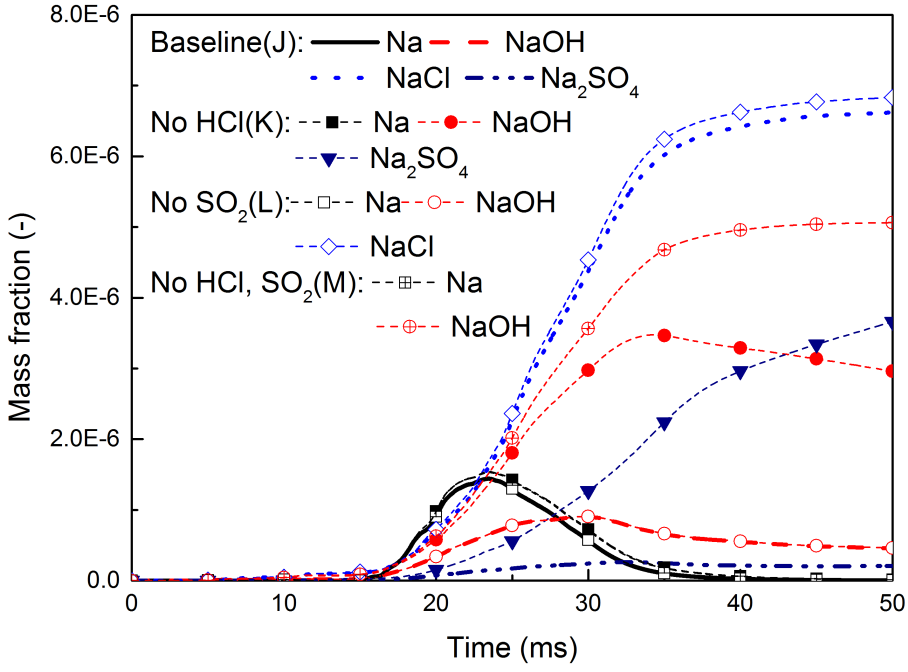

Figure 11. Comparison of time evolutions of the averaged mass fractions of sodium species among Case J (the baseline case), Case K (HCl removed), Case L (SO_2 removed) and Case M (both HCl and SO_2 removed).

4.7. Comparison of sodium emission characteristics in 1D and 2D flames

The 1D premixed flame simulation results (Fig. 2) show that Na has the highest concentration in the sodium products at ϕ = 1.0 and 2.0, which is consistent with the 1D diffusion flame simulation results (Fig. 4). However, under the fuel-lean condition of ϕ = 0.5, the 1D premixed flame results show the major sodium product is NaCl while in the 1D diffusion flame results it is Na. The

discrepancy should be attributed to the fact that the 1D premixed flame is freely propagating while the 1D diffusion flame is strained. From the statistics of the 2D simulation under the baseline condition, NaCl is found to be the major sodium product. The dilution effect of the coflow in the 2D pulverized-coal flame leads to an overall low equivalence ratio of 0.26 (corresponding to a mixture fraction $Z = 0.043$). From the 1D flame results, it can be found that indeed NaCl is the major sodium product under this fuel-lean condition.

5. Conclusions

The transformation characteristics of sodium species in pulverized-coal combustion are numerically investigated via 1D freely propagating premixed and 1D counterflow diffusion flames of coal volatile, and a 2D pulverized-coal flame. Detailed chemistry has been employed for both the combustion of volatile hydrocarbon fuels and the reactions of sodium species. From the 1D premixed flame simulations, it is found that the most significant sodium product is Na under stoichiometric ($\phi = 1.0$) and fuel-rich conditions ($\phi = 2.0$) while it is NaCl under fuel-lean condition ($\phi = 0.5$). NaOH is another major sodium product. HCl is found to have a significant influence on the profile of NaOH in the initial unburned region. It also affects the distribution of Na_2SO_4. However, the effects of SO_2 on the sodium profiles are minor. From the 1D diffusion flame simulations, HCl is found to decrease the concentrations of Na and NaOH in the fuel-rich region with $\phi > 2.0$.

The transformation characteristics of the sodium species in a 2D pulverized-coal flame are then examined. From the instantaneous distribution characteristics, atomic Na is found to have a high concentration in the fuel-rich region. Both Y_{NaOH} and Y_{NaCl} feature a complex distribution over the mixture fraction space, as they reach higher concentrations under both fuel-rich and fuel-lean conditions and decrease to a much lower concentration under the stoichiometric condition. $NaHSO_4$ and Na_2SO_4 are the two main sulfated sodium species which form mainly in the fuel-lean region, but

491 their concentrations are much lower than that of NaCl. From the statistics of the 2D simulation, NaCl
492 is found to be the major sodium product, which is consistent with the 1D simulations. Finally, the
493 parametric study shows that HCl has a much stronger ability to react with sodium species than SO_2.

Acknowledgements

This work was jointly supported by the National Natural Science Foundation of China (51706200), the China Postdoctoral Science Foundation (2018M632460), the Fundamental Research Funds for the Central Universities (2018FZA4012), the Engineering and Physical Sciences Research Council (EPSRC) and the Royal Society of the UK. Y.L. is funded by the Open Topic Exploration Program of the ZJU CEU laboratory. Special thanks are due to Prof. Peter Glarborg of DTU, who provided us the detailed mechanism of alkali metal species. Computing resources were provided by the National Supercomputer Center in Tianjin, China (http://www.nscc-tj.cn).

References

[1] IEA. Key world energy statistics. 2017.

[2] Liu YZ, Wang ZH, Lv Y, Wan KD, He Y, Xia J, et al. Inhibition of sodium release from Zhundong coal via the addition of mineral additives: A combination of online multi-point LIBS and offline experimental measurements. Fuel 2018;212:498-505.

[3] Wu X, Zhang X, Yan K, Chen N, Zhang J, Xu X, et al. Ash deposition and slagging behavior of Chinese Xinjiang high-alkali coal in 3 MWth pilot-scale combustion test. Fuel 2016;181:1191-202.

[4] Wang Ca, Zhu X, Liu X, Lv Q, Zhao L, Che D. Correlations of chemical properties of high-alkali solid fuels: A comparative study between Zhundong coal and biomass. Fuel 2018;211:629-37.

[5] Niu Y, Tan H, Hui Se. Ash-related issues during biomass combustion: Alkali-induced slagging, silicate melt-induced slagging (ash fusion), agglomeration, corrosion, ash utilization, and related countermeasures. Prog. Energy Combust. Sci. 2016;52:1-61.

[6] Jurado N, Simms NJ, Anthony EJ, Oakey JE. Effect of co-firing coal and biomass blends on the gaseous environments and ash deposition during pilot-scale oxy-combustion trials. Fuel 2017;197:145-58.

[7] Liu YZ, Wang ZH, Wan KD, Lv Y, Xia J, He Y, et al. In Situ Measurements of the Release

Characteristics and Catalytic Effects of Different Chemical Forms of Sodium during Combustion of Zhundong Coal. Energy Fuels 2018;32(6):6595-602.

[8] Guo S, Jiang Y, Yu Z, Zhao J, Fang Y. Correlating the sodium release with coal compositions during combustion of sodium-rich coals. Fuel 2017;196:252-60.

[9] Quann RJ, Neville M, Janghorbani M, Mims CA, Sarofim AF. Mineral matter and trace-element vaporization in a laboratory-pulverized coal combustion system. Environ. Sci. Technol. 1982;16(11):776-81.

[10] van Eyk PJ, Ashman PJ, Alwahabi ZT, Nathan GJ. Simultaneous measurements of the release of atomic sodium, particle diameter and particle temperature for a single burning coal particle. Proc. Combust. Inst. 2009;32(2):2099-106.

[11] Liu YZ, Wang ZH, Xia J, Vervisch L, Wan KD, He Y, et al. Measurement and kinetics of elemental and atomic potassium release from a burning biomass pellet. Proc. Combust. Inst. 2019;37(3):2681-8.

[12] He Y, Zhu JJ, Li B, Wang ZH, Li ZS, Aldén M, et al. In-situ measurement of sodium and potassium release during oxy-fuel combustion of lignite using laser-induced breakdown spectroscopy: effects of O2 and CO2 concentration. Energy Fuels 2013;27(2):1123-30.

[13] Liu YZ, He Y, Wang ZH, Xia J, Wan KD, Whiddon R, et al. Characteristics of alkali species release from a burning coal/biomass blend. Appl. Energy 2018;215:523-31.

[14] Wang ZH, Liu YZ, Whiddon R, Wan KD, He Y, Xia J, et al. Measurement of atomic sodium release during pyrolysis and combustion of sodium-enriched Zhundong coal pellet. Combust. Flame 2017;176:429-38.

[15] Liu YZ, He Y, Wang ZH, Wan KD, Xia J, Liu JZ, et al. Multi-point LIBS measurement and kinetics modeling of sodium release from a burning Zhundong coal particle. Combust. Flame 2018;189:77-86.

[16] van Eyk PJ, Ashman PJ, Nathan GJ. Mechanism and kinetics of sodium release from brown coal char particles during combustion. Combust. Flame 2011;158(12):2512-23.

[17] Van Eyk PJ, Ashman PJ, Alwahabi ZT, Nathan GJ. The release of water-bound and organic sodium from Loy Yang coal during the combustion of single particles in a flat flame. Combust. Flame 2011;158(6):1181-92.

[18] Fatehi H, Li ZS, Bai XS, Aldén M. Modeling of alkali metal release during biomass pyrolysis. Proc. Combust. Inst. 2017;36(2):2243-51.

[19] Ekvall T, Andersson K, Leffler T, Berg M. K–Cl–S chemistry in air and oxy-combustion atmospheres. Proc. Combust. Inst. 2017;36(3):4011-8.

[20] Glarborg P, Marshall P. Mechanism and modeling of the formation of gaseous alkali sulfates. Combust. Flame 2005;141(1–2):22-39.

[21] Hindiyarti L, Frandsen F, Livbjerg H, Glarborg P, Marshall P. An exploratory study of alkali sulfate aerosol formation during biomass combustion. Fuel 2008;87(8–9):1591-600.

[22] Garba MU, Ingham DB, Ma L, Porter RTJ, Pourkashnian M, Tan HZ, et al. Prediction of Potassium Chloride Sulfation and Its Effect on Deposition in Biomass-Fired Boilers. Energy Fuels 2012;26(11):6501-8.

[23] Takuwa T, Naruse I. Emission control of sodium compounds and their formation mechanisms during coal combustion. Proc. Combust. Inst. 2007;31 II:2863-70.

[24] Bermúdez A, Ferrín JL, Liñán A, Saavedra L. Numerical simulation of group combustion of pulverized coal. Combust. Flame 2011;158(9):1852-65.

[25] Hashimoto N, Kurose R, Hwang SM, Tsuji H, Shirai H. A numerical simulation of pulverized coal combustion employing a tabulated-devolatilization-process model (TDP model). Combust. Flame 2012;159(1):353-66.

[26] Vascellari M, Cau G. Influence of turbulence–chemical interaction on CFD pulverized coal MILD combustion modeling. Fuel 2012;101:90-101.

[27] Yamamoto K, Murota T, Okazaki T, Taniguchi M. Large eddy simulation of a pulverized coal jet flame ignited by a preheated gas flow. Proc. Combust. Inst. 2011;33(2):1771-8.

[28] Franchetti BM, Cavallo Marincola F, Navarro-Martinez S, Kempf AM. Large eddy simulation of a pulverised coal jet flame. Proc. Combust. Inst. 2013;34(2):2419-26.

[29] Rabaçal M, Franchetti BM, Marincola FC, Proch F, Costa M, Hasse C, et al. Large Eddy Simulation of coal combustion in a large-scale laboratory furnace. Proc. Combust. Inst. 2015;35(3):3609-17.

[30] Wan KD, Xia J, Wang ZH, Wrobel LC, Cen KF. Online-CPD-coupled large-eddy simulation of pulverized-coal pyrolysis in a hot turbulent nitrogen jet. Combust. Sci. Technol. 2017;189(1):103-31.

[31] Wen X, Luo Y, Luo K, Jin H, Fan J. LES of pulverized coal combustion with a multi-regime flamelet model. Fuel 2017;188:661-71.

[32] Rieth M, Clements AG, Rabaçal M, Proch F, Stein OT, Kempf AM. Flamelet LES modeling of coal combustion with detailed devolatilization by directly coupled CPD. Proc. Combust. Inst. 2017;36(2):2181-9.

[33] Wan KD, Xia J, Wang ZH, Pourkashanian M, Cen KF. Large-eddy Simulation of Pilot-assisted Pulverized-coal Combustion in a Weakly Turbulent Jet. Flow Turbul. Combust. 2017;99(2):531-50.

[34] Wan KD, Xia J, Vervisch L, Liu YZ, Wang ZH, Cen KF. Modelling alkali metal emissions in large-eddy simulation of a preheated pulverised-coal turbulent jet flame using tabulated chemistry. Combust. Theory Model. 2018;22(2):203-36.

[35] Hara T, Muto M, Kitano T, Kurose R, Komori S. Direct numerical simulation of a pulverized coal jet flame employing a global volatile matter reaction scheme based on detailed reaction mechanism. Combust. Flame 2015;162(12):4391-407.

[36] Muto M, Yuasa K, Kurose R. Numerical simulation of ignition in pulverized coal combustion

with detailed chemical reaction mechanism. Fuel 2017;190:136-44.

[37] Wan KD, Vervisch L, Xia J, Domingo P, Wang ZH, Liu YZ, et al. Alkali metal emissions in an early-stage pulverized-coal flame: DNS analysis of reacting layers and chemistry tabulation. Proc. Combust. Inst. 2019;37(3):2791-9.

[38] Iisa K, Lu Y, Salmenoja K. Sulfation of Potassium Chloride at Combustion Conditions. Energy Fuels 1999;13(6):1184-90.

[39] Kazakov A, Frenklach M. Reduced reaction sets based on GRI-Mech 1.2. 1994. (http://www.me.berkeley.edu/drm/).

[40] Grant DM, Pugmire RJ, Fletcher TH, Kerstein AR. Chemical-Model of Coal Devolatilization Using Percolation Lattice Statistics. Energy Fuels 1989;3(2):175-86.

[41] Goodwin DG, Moffat HK, Speth RL. Cantera: An object-oriented software toolkit for chemical kinetics, thermodynamics, and transport processes. 2017. (http://www.cantera.org). Version 2.3.0.

[42] Knappstein R, Kuenne G, Ketelheun A, Köser J, Becker L, Heuer S, et al. Devolatilization and volatiles reaction of individual coal particles in the context of FGM tabulated chemistry. Combust. Flame 2016;169:72-84.

[43] Miller RS, Bellan J. Direct numerical simulation of a confined three-dimensional gas mixing layer with one evaporating hydrocarbon-droplet-laden stream. J. Fluid Mech. 1999;384:293-338.

[44] Ranz WE, Marshall WR. Evaporation from drops. Chem. Eng. Prog. 1952;48(3):141-6.

[45] Chandrasekhar S. Radiative transfer. New York: Dover Publications; 1960.

[46] Wan KD, Wang ZH, He Y, Xia J, Zhou ZJ, Zhou JH, et al. Experimental and modeling study of pyrolysis of coal, biomass and blended coal–biomass particles. Fuel 2015;139:356-64.

[47] Smith TF, Shen ZF, Friedman JN. Evaluation of Coefficients for the Weighted Sum of Gray Gases Model. J. Heat Transfer 1982;104(4):602-8.

[48] Pierce CD, Moin P. Progress-variable approach for large-eddy simulation of non-premixed turbulent combustion. J. Fluid Mech. 2004;504:73-97.

[49] Desjardins O, Blanquart G, Balarac G, Pitsch H. High order conservative finite difference scheme for variable density low Mach number turbulent flows. J. Comput. Phys. 2008;227(15):7125-59.

[50] Domingo P, Vervisch L, Réveillon J. DNS analysis of partially premixed combustion in spray and gaseous turbulent flame-bases stabilized in hot air. Combust. Flame 2005;140(3):172-95.

[51] Reveillon J, Vervisch L. Analysis of weakly turbulent dilute-spray flames and spray combustion regimes. J. Fluid Mech. 2005;537:317-47.

Figure captions

Figure 1. Schematic diagram of computational configuration.

Figure 2. Sodium species distribution versus distance along the 1D premixed volatile flame at equivalence ratio ϕ = 0.5 (a), ϕ = 1.0 (b) and ϕ = 2.0 (c). The heat release zone is zoomed in and shown on the left side while the overall flame is shown on the right side.

Figure 3. Comparison of sodium species distribution versus distance along the 1D premixed volatile flame between Case A (the baseline case), Case B (HCl removed), Case C (SO_2 removed) and Case D (both HCl and SO_2 removed) at equivalence ratio ϕ = 0.5 (a), ϕ = 1.0 (b) and ϕ = 2.0 (c).

Figure 4. Comparison of sodium species distribution in the mixture fraction space of the 1D diffusion volatile flame among Case E (the baseline case), Case F (HCl removed), Case G (SO_2 removed) and Case H (both HCl and SO_2 removed).

Figure 5. Time evolutions of instantaneous distributions of the (a) gas temperature and particle burnout, (b) OH mass fraction, (c) Na mass fraction, (d) NaCl mass fraction and (e) flame index and particle temperature.

Figure 6. Time evolutions of instantaneous distribution of the flame index and particle temperature from t = 14.0 ms to t = 15.0 ms.

Figure 7. Instantaneous distributions of the equivalence ratio (ϕ), the mass fractions of HCl, SO_2 and all the twelve sodium species at t = 20 ms. The isoline of ϕ = 1 is superimposed.

Figure 8. Scatter plots of instantaneous mass fractions of Na, NaCl, NaOH, $NaHSO_4$, Na_2SO_4 and Na_2Cl_2 against Z at t = 20 ms. Blue solid line and red dash line are the sodium profiles obtained from 1D counterflow diffusion flames, corresponding to the lowest (23 s^{-1}) and highest strain rates (11318 s^{-1}).

Figure 9. Time evolutions of the mean mass fractions of OH, HCl, SO_2 and Z_{vol} averaged over the 2D computational domain.

Figure 10. Time evolutions of the averaged mass fractions of Na, NaOH, NaCl, $NaHSO_4$, Na_2SO_4 and Na_2Cl_2, and the averaged gas temperature.

Figure 11. Comparison of time evolutions of the averaged mass fractions of sodium species among Case J (the baseline case), Case K (HCl removed), Case L (SO_2 removed) and Case M (both HCl and SO_2 removed).

Color figures can be used for the online PDF version and the gray style for hardcopy reproduction.